Evaluation of the VMF3-FC and prior variance modeling: implications for PPP/PPP-IAR performance

Xiaoting Lei[1,2] · Jun Tao[1,2] · Tianyu Yang[3] · Gaojian Zhang[1,2] · Qile Zhao[1,2,4] · Jing Guo[1,2]

Abstract

Precise modeling of the troposphere is essential for applications such as radio signal processing and weather forecasting. VMF3-FC (Vienna Mapping Functions 3 Forecast) provides high-precision real-time products, including the zenith hydrostatic delay (ZHD) and zenith wet delay (ZWD). In this study, VMF3-FC products were evaluated from 2019 to 2023 using global IGS-ZTD data from 523 IGS stations. The five-year global average RMS values of the VMF3-FC products were 1.53 cm for site-wise, 1.63 cm for $1 \times 1°$ grid-wise, and 2.23 cm for $5 \times 5°$ grid-wise. A highly accurate a priori variance model was proposed considering the distribution characteristics of the VMF3-FC error. The model residuals for different VMF3-FC products as 0.27, 0.32 and 0.57 cm, respectively. To validate the effectiveness of the priori variance model, globally distributed stations were selected to perform ZTD-augmented PPP with integer ambiguity resolution (PPP-IAR) reconvergence experiments. A comparative analysis was carried out on the PPP-IAR performances with and without true a priori variance, fitted variance, and empirical variance constraints. The best performance was achieved using the true variance, followed closely by the fitted variance from latitudinal fitting, where both these performances were considerably greater than that achieved using the empirical variance. Specifically, compared to the unconstrained scenario, the use of empirical variance, fitted variance, and true variance constraints respectively reduced the PPP-IAR convergence time by 7.1, 8.9 and 9.5%, and increased the ambiguity resolution success rate by 1.34, 1.49 and 1.49%. The corresponding improvement in the pre-convergence accuracy was 16.5, 17.3 and 17.1%, respectively, in the vertical component. These findings confirm that the fitted variance closely approximates the statistically determined true variance, demonstrating the global effectiveness and reliability of the proposed fitting method. Thus, the fitted variance can replace empirical values as the a priori variance used in VMF3-FC products to enhance real-time applications.

Keywords VMF3-FC · Prior variance modeling · Accuracy evaluation · ZTD-augmented PPP-IAR

Introduction

Tropospheric delay is a crucial source of error in global navigation satellite system (GNSS) positioning (Nafisi et al. 2012; Teunissen and Khodabandeh 2015). The tropospheric delay is typically divided into the zenith tropospheric delay (ZTD), horizontal gradients, and a mapping function. The ZTD comprising the zenith hydrostatic delay (ZHD) and the zenith wet delay (ZWD). Horizontal gradients describe the east–west and north–south variations of ZTD, while mapping functions are used to convert slant path delays to zenith delays. Various tropospheric meteorological models have been developed to achieve tropospheric calculations (Santerre 1991). These models include the Hopfield model (Hopfield 1969), Saastamoinen model (Saastamoinen 1972), Black model (Black 1978) and askne-nordius model (ANM)

✉ Jun Tao
  jtaowhu@whu.edu.cn

1   GNSS Research Center, Wuhan University, No. 129 Luoyu Road, Wuhan 430079, China

2   School of Geodesy and Geomatics, Wuhan University, No. 129 Luoyu Road, Wuhan 430079, China

3   School of Geomatics, Liaoning Technical University, 47 Zhonghua Road, Fuxin 123000, China

4   Collaborative Innovation Center of Geospatial Technology, Wuhan University, No. 129 Luoyu Road, Wuhan 430079, China

(Askne and Nordius 1987). The Saastamoinen model is widely employed for calculating the ZHD because of its ability to achieve optimal accuracy, whereas the ANM is used to calculate the ZWD. The Global Pressure and Temperature (GPT), developed using atmospheric reanalysis data from the European Centre for Medium-Range Weather Forecasts (ECMWF), is used to calculate meteorological parameters such as global pressure and temperature (Böehm et al. 2007; Hersbach et al. 2020). The GPT model assumes that meteorological parameters at individual grid points exhibit both annual and semi-annual cycles, and employs second-order Fourier functions for fitting and modeling. Users can calculate the meteorological parameters for any grid point based on the Day of Year (DOY) and the coefficients provided by GPT. Then, they can use the Saastamoinen and ANM models to compute the ZHD and ZWD, respectively. Finally, they can use bilinear interpolation to obtain the ZTD value for their specific station (Lagler et al. 2013; Böhm et al. 2015; Landskron and Böhm 2018). The most commonly used method for ZTD correction involves the use of the GPT to obtain atmospheric parameters, followed by the calculation of the ZHD and ZWD via the Saastamoinen and ANM models, respectively. The GPT model calculates the ZHD remarkably accurately, whereas empirical models are less effective in providing accurate ZWD corrections (Berrada Baby et al. 1988; Bevis et al. 1992; Yang et al. 2021b; Zhu et al. 2022).

In PPP processing, empirical models are typically applied for tropospheric corrections, and tropospheric wet delay parameters are set to estimate residual ZWD (Li et al. 2022; Lyu et al. 2022). Consequently, the ZWD parameter estimation directly affects PPP convergence speed, while process noise and a priori variance are critical parameters in ZWD estimation (Teunissen and Khodabandeh 2015; Psychas et al. 2022). Hadas et al. (2017) calculated tropospheric random walk process noise (RWPN) using historical or real-time global Numerical Weather Model (NWM) data. Experimental results showed that the derived tropospheric RWPN improved the estimation accuracy of ZTD by 10%. Building on Hadas' work, Wu et al. (2023) enhanced both the computational efficiency and accuracy of the model by developing a Global Random Walk Process Noise Model (GRM) based on a decade of NWM data. The results demonstrated that GRM delivered a 10% improvement in performance compared to the original RWPN. Current research on determining the prior variance of tropospheric models remains limited. For instance, the often-used Optimal Fitting Coefficients (OFC) model constructs tropospheric models via polynomial least-squares fitting and suggests using a 3σ value as the prior variance. However, the inability of many tropospheric models to provide σ values significantly limits the practical applicability of this approach. Cui et al. (2022) enhanced PPP-IAR by utilizing the root mean square (RMS)

statistics from Modified OFC (MOFC) as the model variance. This approach is viable because MOFC is a regional model, enabling a single RMS value to characterize small regional prior variance. However, using a empiric value to represent the global model accuracy is evidently improper. Yang et al. (2023) partitioned the global domain into clusters and performed accuracy modeling for empirical tropospheric models (e.g., GPT2w) based on these clusters, thereby defining the prior accuracy of the models. However, the comparatively limited accuracy of such empirical models restricts their capacity to improve PPP-IAR performance effectively. With the release of tropospheric prediction products, numerous researchers have also used these products to enhance PPP positioning (Lu et al. 2024; Tao et al. 2024; Gao et al. 2024). Although the experimental results indicate improved positioning performance, the empirical variances employed are evidently not the most rational method for specifying prior variances.

The Vienna Mapping Functions 3 (VMF3) product predicts the ZTD by fitting ECMWF data. Grid data with global horizontal resolutions of $5\times5°$ and $1\times1°$ are provided one day in advance, enabling ZTD retrieval at any location through bilinear interpolation (Re3data.Org 2016). The accuracy of ZTD prediction products have been evaluated in several studies, demonstrating that predictive models substantially outperform empirical models. For example, Yuan et al. (2019) showed that the ZTD predicted by VMF1-FC was highly consistent with the CODE ZTD. Both the VMF1-FC ZTD and real-time PPP (RTPPP) methods achieved RMS ZTD errors below 1 cm, considerably outperforming the GPT2 and GPT2W models. Subsequent studies by Osah et al. (2021) and Zhang et al. (2024) on VMF3-FC products in West Africa and China revealed that the VMF3-FC was considerably more accurate than the GPT3 model. Li et al. (2024) reported a minimal difference between the TUW-VMF3 and GFZ-VMF3 products. The high accuracy of these ZTD prediction products has led to their application in various fields. For example, Sun et al. (2021) utilized VMF1-FC and VMF3-FC to retrieve the precipitable water vapor (PWV). The RMS of the PWV obtained using VMF3-FC was only 0.49 cm.

The VMF3-FC product has not been comprehensively globally evaluated in previous studies, and an empirical a priori accuracy of 2–3 cm can obtained through regional accuracy assessment (Yang et al. 2021a; Zhang et al. 2024). This priori accuracy reduces the practicality of using the product in real-time positioning applications. In this study, both site-wise and grid-wise VMF3-FC products are evaluated via International GNSS Service ZTD (IGS-ZTD). An a priori variance model for VMF3-FC is established on the basis of the evaluation results and applied to PPP solutions.

In this paper, the VMF3-FC ZTD calculation and ZTD-augmented PPP-IAR model are first described, and the data and

processing strategies employed are detailed. Next, the distribution characteristics of the VMF3-FC errors are analyzed and used to develop an a priori variance model. The accuracies of the VMF3-FC product and the proposed variance model are then validated via data from a globally distributed network of IGS stations. Finally, the findings are summarized.

Methods

In this section, the VMF3-FC calculation method is first introduced, followed by a detailed derivation of the ZTD-enhanced PPP/PPP-IAR algorithm.

VMF3-FC ZTD calculation

The slant tropospheric delay $T_r^{s,g}$ in VMF3-FC can be calculated using the ZHD, ZWD, and their mapping function as follows:

$$T_r^{s,g} = m_{h,r}^{s,g} \cdot T_{h,r} + m_{w,r}^{s,g} \cdot T_{w,r} \tag{1}$$

where $T_{h,r}$ and $T_{w,r}$ represent the ZHD and ZWD, respectively; $m_{h,r}^{s,g}$ and $m_{w,r}^{s,g}$ are the corresponding mapping functions; the superscripts s and g correspond to the satellite and constellation identifiers, respectively, and the subscript r refers to the receiver. VMF3-FC provides the ZHD and ZWD but only at grid points with a temporal resolution of 6 h and a spatial resolution of 1° or 5°. Therefore, when deriving ZHD and ZWD at specific sites using VMF3-FC, users must perform additional interpolations. The computation process consists of three main steps: temporal interpolation, height conversion, and spatial interpolation.

Initially, the ZHD and ZWD values are linearly interpolated to obtain the VMF3-FC ZHD and ZWD for the current moment. The interpolation is carried out using Formula (2):

$$T_{h,t_c} = T_{h,t_1} + \left(\frac{T_{h,t_2} - T_{h,t_1}}{t_2 - t_1} \right) \cdot (t_c - t_1) \tag{2}$$

where t_c represents the current time, and t_1 and t_2 denote the times provided by the product immediately before and after t_c, respectively. All other variables have been previously defined. The same time interpolation method is used to calculate the ZWD as the ZHD and is not given here.

The ZHD mainly depends on the pressure. It is essential to convert ZHD values from the VMF3-FC grid points into pressure parameters to maintain precision in height conversion. This conversion is given by Formula (3):

$$P_{grid} = \frac{T_{h,grid}}{0.0022768} \cdot \left(1 - 0.00266 \cdot \cos(2 \cdot L_{grid}) - 0.28 \cdot 10^{-6} \cdot h_{grid} \right) \tag{3}$$

where P_{grid} represents the pressure at a grid point and the variables L_{grid} and h_{grid} represent the latitude and height of the grid points, respectively. The values for L_{grid} and h_{grid} can be obtained from the coordinate file available at https://vmf.geo.tuwien.ac.at/station_coord_files/.

The pressure at the grid-point height h_{grid} is converted to that at the user station height h_{site} using the following formula (Kouba 2008):

$$P_{site} = P_{grid} \cdot \left(1 - 0.0000226 \cdot (h_{site} - h_{grid}) \right)^{5.225} \tag{4}$$

The ZHD at the user station height is calculated using the corresponding pressure parameters and the latitude information from the grid points as follows (Saastamoinen 1972):

$$T_{h,site} = 0.0022768 \cdot P_{site} \cdot \frac{1}{1 - 0.00266 \cdot \cos(2 \cdot L_{site}) - 0.28 \cdot 10^{-6} \cdot h_{site}} \tag{5}$$

The ZWD depends mainly on the water vapor pressure and can be directly converted via an exponential function. The conversion formula is as follows:

$$T_{w,site} = T_{w,grid} \cdot \exp\left(-(h_{site} - h_{grid})/2000 \right) \tag{6}$$

The ZHD and ZWD calculated at the height of the user station are subjected to 2D bilinear interpolation to calculate them at the horizontal location of the user station. Bilinear interpolation is commonly used for horizontal interpolation, and the same method is used to interpolate ZHD and ZWD values. This method is described here using the ZHD as an example. Given four grid points $(x_1, y_1), (x_2, y_1), (x_1, y_2)$ and (x_2, y_2) and the user station located at (x_s, y_s), the bilinear interpolation formula for estimating the ZHD at (x_s, y_s) is as follows (Accadia et al. 2003):

$$\begin{cases} T_{h,site} = \frac{y_2 - y_s}{y_2 - y_1} \cdot T_{h,grid_{s,1}} + \frac{y_s - y_1}{y_2 - y_1} \cdot T_{h,grid_{s,2}} \\ T_{h,grid_{s,1}} = \frac{x_2 - x_s}{x_2 - x_1} \cdot T_{h,grid_{1,1}} + \frac{x_s - x_2}{x_2 - x_1} \cdot T_{h,grid_{2,1}} \\ T_{h,grid_{s,2}} = \frac{x_2 - x_s}{x_2 - x_1} \cdot T_{h,grid_{1,2}} + \frac{x_s - x_2}{x_2 - x_1} \cdot T_{h,grid_{2,2}} \end{cases} \tag{7}$$

ZTD-augmented PPP-IAR model

The a priori ZTD is typically computed using the GPT2w model, which provides centimeter-level estimates (Du et al. 2020). The a priori ZTD is incorporated into the observation equation, and the ZTD residual is estimated by incorporating additional parameters. The undifferenced and uncombined (UDUC) GNSS linearized equations are as follows:

$$
\begin{cases}
E\{\delta p_{i,r}^{s,g}\} = H_r^{s,g}\Delta x + \widetilde{\delta t}_r^{g} + \mu_i^{\cdot g}\widetilde{I}_r^{s,g} + m_{w,r}^{s,g}\Delta T_{w,r} + M_{i,r}^{s,g} \\
E\{\delta \emptyset_{i,r}^{s,g}\} = H_r^{s,g}\Delta x + \widetilde{\delta t}_r^{g} - \mu_i^{\cdot g}\widetilde{I}_r^{s,g} + m_{w,r}^{s,g}\Delta T_{w,r} + \lambda_i^{g}\widetilde{N}_{i,r}^{s,g}
\end{cases}
\tag{8}
$$

where

$$
\begin{cases}
\widetilde{\delta t}_r = \delta t_r + \dfrac{\mu_2^{\cdot g}}{\mu_2^{\cdot g}-\mu_1^{\cdot g}}d_{1,r} - \dfrac{\mu_1^{\cdot g}}{\mu_2^{\cdot g}-\mu_1^{\cdot g}}d_{2,r} \\
\widetilde{I}_r^{s,g} = I_r^{s,g} - \dfrac{\gamma_1}{\gamma_2-\gamma_1}\left(d_{1,r}^{s,g} - d_{2,r}^{s,g}\right) \\
M_{i,r}^{s,g} = \dfrac{\mu_i^{\cdot g}-\mu_1^{\cdot g^2}}{\mu_2^{\cdot g}-\mu_1^{\cdot g}}\left(d_{1,r}-d_{2,r}\right) - \left(d_{1,r}-d_{i,r}\right) - \left(\dfrac{\mu_i^{\cdot g}-\mu_1^{\cdot g}}{\mu_2^{\cdot g}-\mu_1^{\cdot g}}\left(d_1^{s,g}-d_2^{s,g}\right) - \left(d_1^{s,g}-d_i^{s,g}\right)\right) \\
\widetilde{N}_{i,r}^{s} = N_{i,r}^{s,g} + d_{\emptyset_{i,r}} - \dfrac{1}{\lambda_i^{g}}\left(\dfrac{\mu_i^{\cdot g}+\mu_1^{\cdot g}}{\mu_2^{\cdot g}-\mu_1^{\cdot g}}d_{1,r}^{s,g} - \dfrac{\mu_i^{\cdot g}+\mu_2^{\cdot g}}{\mu_2^{\cdot g}-\mu_1^{\cdot g}}d_{2,r}^{s,g}\right) \\
d_{*,r}^{s,g} = d_{*,r} - d_{*}^{s,g}
\end{cases}
\tag{9}
$$

The terms in the equation given above are defined here. $E\{\bullet\}$ denotes the expectation operator. $\delta p_{i,r}^{s,g}$ and $\delta \phi_{i,r}^{s,g}$ are the observed-minus-computed (OMC) values of the code and phase observations, respectively. The OMC encompasses prior correction values for a range of errors. These values include the a priori ZTD (Byun and Bar-Sever 2009; Tao et al. 2024), the geometric distance between the known satellite and station coordinates, and corrections for antenna phase centers and phase windup effects. In particular, $\delta \phi_{i,r}^{s,g}$ includes a correction for the observable-specific signal bias (OSB). The subscript i refer to the frequency identifier, which takes values of 1, 2, and 3. $H_r^{s,g}$ is a vector of unit length. Δx is the coordinate increment relative to the initial coordinates; $I_r^{s,g}$ is the ionospheric delay at the first frequency, and the scale factor $\mu_i^{\cdot g} = \left(f_1^{g}/f_i^{g}\right)^2$ is the corresponding coefficient for the frequency i. $N_{i,r}^{s,g}$ is the integer ambiguity, and λ_i^{g} is the wavelength. $d_{p_{i,r}^{g}}$ and $d_{p_i^{s,g}}$ represent the code hardware delays at the receiver and satellite ends, respectively. $d_{\phi_{i,r}^{g}}$ and $d_{\phi_i^{s,g}}$ represent the station- and satellite-related phase hardware delays, respectively. In particular, $M_{i,r}^{s,g}$ represents the hardware delay at the third frequency. When only two frequencies are used, the value of $M_{i,r}^{s,g}$ is set to 0.

The VMF3-FC tropospheric constraints are incorporated into PPP-IAR. Considering that the GPT2w model is used for tropospheric correction during the solution process, the discrepancy between VMF3-FC and GPT2w is utilized to constrain the tropospheric parameters $\Delta T_{w,r}$:

$$
\begin{cases}
E\left\{\delta p_{i,r}^{s,g}\right\} = H_r^{s,g}\Delta x + \widetilde{\delta t}_r^{g} + \mu_i^{\cdot g}\widetilde{I}_r^{s,g} + m_{w,r}^{s,g}\Delta T_{w,r} + M_{i,r}^{s,g} \\
E\left\{\delta \phi_{i,r}^{s,g}\right\} = H_r^{s,g}\Delta x + \widetilde{\delta t}_r^{g} - \mu_i^{\cdot g}\widetilde{I}_r^{s,g} + m_{w,r}^{s,g}\Delta T_{w,r} + \lambda_i^{g}\widetilde{N}_{i,r}^{s,g} \\
\Delta T_{w,r} = T_{h,fc} + T_{w,fc} - T_{h,gpt} - T_{w,gpt}
\end{cases}
\tag{10}
$$

The subscripts *fc* and *gpt* represent VMF3-FC and GPT2w, respectively. Therefore, $T_{h,fc}$ and $T_{w,fc}$ represent the ZHD and ZWD computed using VMF3-FC, respectively.

The stochastic model of the GNSS observation and constraint equations is as follows:

$$
Q^2 = \operatorname{diag}(Q_P^2, Q_{\emptyset}^2, Q_T^2)
\tag{11}
$$

where Q_P and $Q_{\emptyset}$ are the observation noises for the code and phase observations and are normally set to 0.3 m and 0.003 m, respectively. Q_T is the a priori noise for ZTD virtual observations and needs to be determined.

Data

First, the data sources used to evaluate VMF3-FC are presented. Next, a statistical analysis is performed of the IGS-ZTD data from 2019 to 2023. Finally, the data evaluation method, solution strategy, and experimental procedure are presented.

Data collection

The VMF3 model provides two distinct types of tropospheric products: empirical and discrete. The discrete category encompasses both VMF3-OP and VMF3-FC. VMF3-OP is a post-ZTD product that provides the previous day's results in grid-wise ($1 \times 1°$ and $5 \times 5°$ resolutions) and site-wise formats at approximately 18:30 UTC every day. These results include the ZHD, the ZWD, and meteorological parameters. Similarly, VMF3-FC provides grid-wise data and site-wise predictions for real-time users generated from ECMWF forecast data that is updated daily at 9:30 UTC. The grid-wise product delivers ZHD and ZWD data at four key times each day, which can be subjected to linear and bilinear interpolation to obtain the corresponding data at specific times and locations (Yang et al. 2021a; Niell 1996; Kouba 2008). In this study, VMF3-FC data from 2019 to 2023 were utilized for accuracy evaluation and variance modeling.

IGS-ZTD products are obtained through postprocessing solutions, with accuracies ranging from 1.5 to 5 mm (Byun and Bar-Sever 2009; Noll 2010). Therefore, the IGS-ZTD was selected as the reference ZTD value used in this study

to verify the accuracy of VMF3-FC. The IGS-ZTD data from the IGS data center for the period from 2019 to 2023 were downloaded and processed. The temporal resolution was 5 min for IGS-ZTD and 6 h for VMF3-FC, making it necessary to align the data temporally. The aligned temporal resolution of IGS-ZTD was 6 h, and IGS-ZTD values were extracted at 00:00, 06:00, 12:00, and 18:00 each day (Re3data.Org 2016).

A statistical analysis of the effectiveness of IGS-ZTD from 2019 to 2023 was conducted. Figure 1 is a map that was generated to display the effective quantity of the IGS-ZTD data.

The statistical analysis of the VMF3-FC product indicated missing the $1 \times 1°$ and $5 \times 5°$ resolution grid products for 00:00 on December 18, 2023. However, the VMF3-FC site-wise product and the VMF3-OP product were functioning normally at that time. The data for other times in the VMF3-FC product were not affected and had normal values.

Data processing strategy

The IGS-ZTD product provides only the ZTD at IGS sites, making it difficult to evaluate the ZHD and ZWD separately. To evaluate the ZHD and ZWD of VMF3-FC separately, the pressure and temperature data from the VMF3-OP site-wise product were used to calculate the ZHD, whereas the IGS-ZWD was extracted from the IGS-ZTD as the reference for the VMF3-FC ZWD. The pressure and temperature in VMF3-OP are postprocessed products, ensuring the accuracy of the ZHD calculation.

The following accuracy metrics were calculated for both the ZTD and ZWD: the mean error (MEAN), mean absolute error (MAE), standard deviation (STD), and RMS.

$$
\begin{cases}
\text{MEAN} = (X_1 + X_2 + \cdots + X_n)/n \\
\text{MAE} = (|X_1| + |X_2| + \cdots + |X_n|)/n \\
\text{RMS} = \sqrt{(X_1^2 + X_2^2 + \cdots + X_n^2)/n} \\
\text{STD} = \sqrt{\left[(X_1 - \text{MEAN})^2 + (X_2 - \text{MEAN})^2 + \cdots + (X_n - \text{MEAN})^2\right]/n}
\end{cases}
\tag{12}
$$

The strategy employed for the PPP-IAR solution is summarized in Table 1.

Figure 2 illustrates the evaluation procedure for VMF3-FC. In this procedure, the accuracy of the ZHD and ZWD of VMF3-FC is first assessed respectively. Then, an a priori model is constructed based on the obtained accuracy information. Finally, the GNSS observation is used to validate this model.
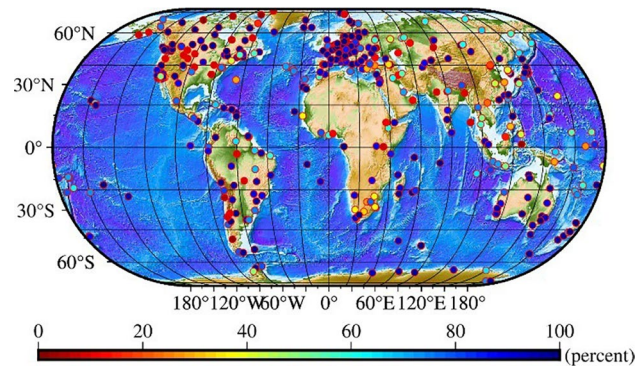
Fig. 1 Distribution of IGS stations and statistics for the percentage of IGS ZTD from 2019–2023

Results

The precision of VMF3-FC products is evaluated, followed by a prior variance modeling on the basis of the error distribution characteristics. Subsequently, globally distributed stations are selected to validate the accuracy of the prior variance model.

Evaluation of VMF3-FC accuracy

The IGS-ZTD is used as the reference for the VMF3-FC ZTD product. However, IGS does not provide a ZWD product, hence it is not possible to directly obtain reference values for the VMF3-FC ZWD product. Fortunately, VMF3-OP is derived from ECMWF reanalysis products and provides pressure and ZHD for each IGS station, with ZHD accuracy reaching the millimeter level (Liu 2020; Huang et al. 2021). Therefore, the IGS-ZWD is derived by subtracting the VMF3-OP ZHD from the IGS-ZTD products to serve

as a reference for evaluating the accuracy of the VMF3-FC ZWD products. The differences between the VMF3-FC ZTD, ZWD and IGS reference values are calculated by differencing. The five-year deviations for each IGS station are statistically analyzed, and the corresponding MEAN, MAE, STD, and RMS values are computed.

Figure 3 shows that the MEAN of the VMF3-FC site-wise ZTD globally approaches zero, indicating that the VMF3-FC site-wise ZTD is uniformly distributed and nearly unbiased around zero. The MAE, STD, and RMS are correlated with the geographical location, where the smallest errors are
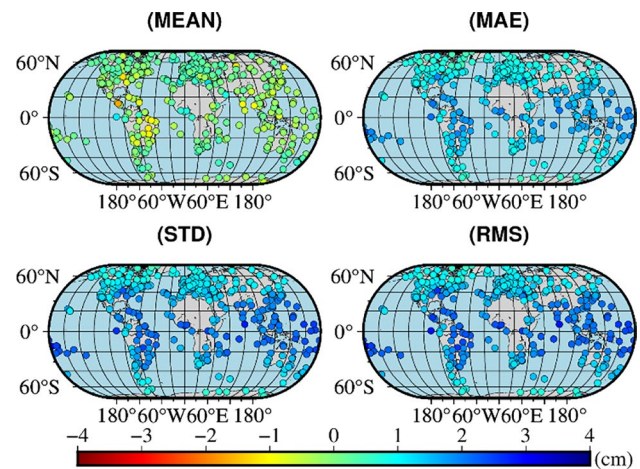
Table 1 Summary of the data processing strategy

Items	Description
Frequency	GPS: L1/L2/L5; GAL: E1/E5a/E5b; BDS-2: B1I/B3I/B2b BDS-3: B1I/B3I/B2a
Observations	Undifferenced and uncombined
Intervals	30 s for PPP evaluation
Elevation mask	7°
Cycle slip detection	Turbo-Edit algorithm and LLI (Blewitt 1990)
Stochastic model	An elevation-dependent function
$\sigma_\theta = \begin{cases} 1 & \theta > 30° \\ 2 \cdot \sin^2\theta & \theta \le 30° \end{cases}$	
Receiver code bias	Estimated as piecewise constant with a sigma of 10 m and process noise of $0.03 \text{m}/\sqrt{\text{hour}}$
Satellite orbit	Fixed as the real-time orbit products of WHU (Xu et al. 2024)
Satellite DCB	WHU final DCB products (Zhang and Zhao 2018)
Satellite clocks and OSB	Fixed as global re-estimated real-time products
Coordinates	Estimated as white noise for PPP/PPP-IAR
Ambiguity	Constant, cascading MLAMBDA ambiguity fixing for PPP-IAR (Tao et al. 2022)
Troposphere	The a priori correction is performed using the GPT2w model, whereas the residual ZWD is estimated as random-walk noise with an a priori sigma of 0.1 m and process noise of $0.02\text{m}/\sqrt{\text{hour}}$ in PPP/PPP-IAR and is constrained to the VMF3-FC value in troposphere augmented PPP/PPP-IAR
Ionosphere	Estimated as a random walk with an a priori sigma of 30 m and process noise of $10\text{m}/\sqrt{30\text{s}}$
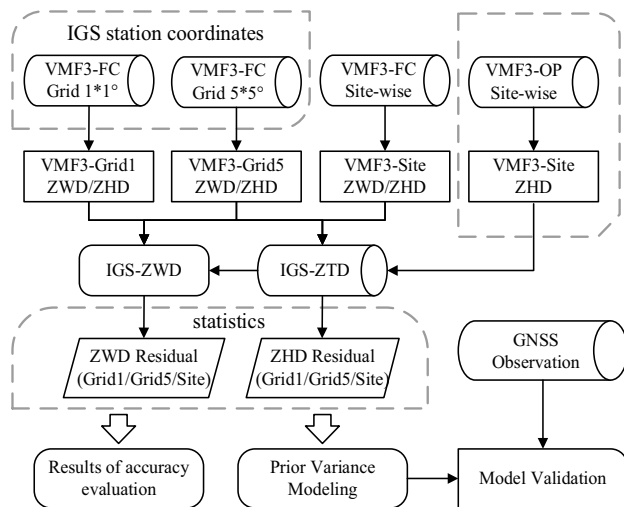
Fig. 2 The workflow for VMF3-FC evaluation and modeling

Fig. 3 Statistical accuracy of the VMF3-FC site-wise ZTD product obtained using the IGS-ZTD as a reference value, where the MEAN, MAE, STD and RMS are calculated over a five-year period

incurred in the polar regions and the errors increase as the latitude decreases. The errors are highest near the equator.

Figure 4 shows that the ZWD error distribution closely tracks that of the ZTD. This result suggests that the errors related to the geographical location are primarily caused by the ZWD, whereas the ZHD error is minimal and uniformly distributed across the globe. The primary factors influencing the variation in the ZWD with the latitude are probably the water vapor content and tropical meteorological activities.

For example, convective activity and tropical cyclones are driven by elevated temperatures in equatorial regions. These factors lead to fluctuations in the water vapor being more pronounced in low-latitude regions than in high-latitude regions.

Bilinear interpolation is performed on the $1 \times 1°$ grid VMF3-FC product to derive the ZTD and ZWD at the IGS station, and the accuracy of the results are assessed. The statistical results spanning five years are plotted and are
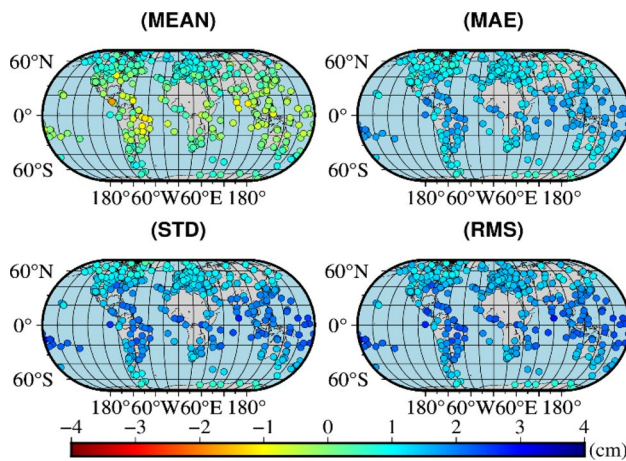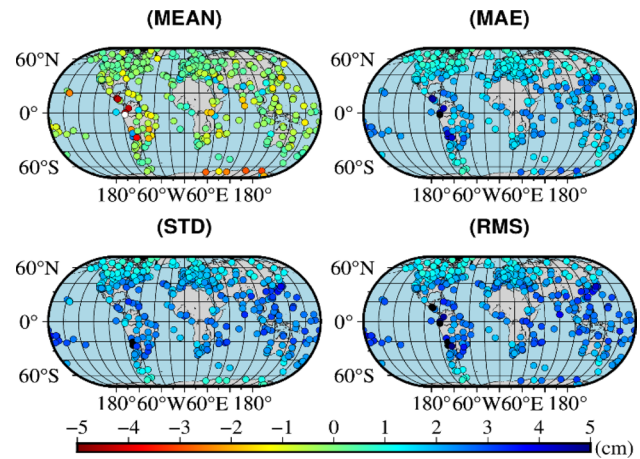
Fig. 4 Statistical accuracy of the VMF3-FC site-wise ZWD product obtained using the ZWD separated from IGS-ZTD as a reference, where the MEAN, MAE, STD and RMS are calculated over a five-year period
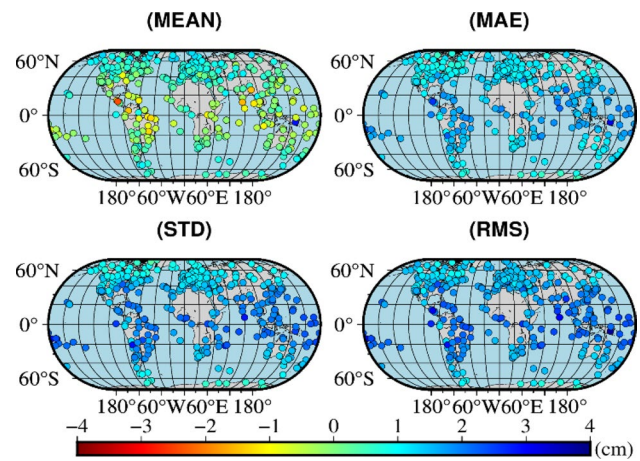
Fig. 6 Statistical accuracy of the VMF3-FC $1 \times 1°$ grid-wise ZWD product obtained using the ZWD separated from the IGS-ZTD as a reference, where the MEAN, MAE, STD and RMS are calculated over a five-year period
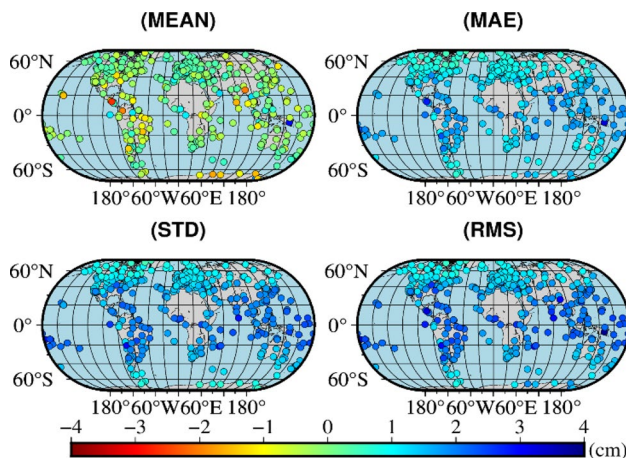
Fig. 5 Statistical accuracy of the VMF3-FC $1 \times 1°$ grid-wise ZTD product obtained using the IGS-ZTD as a reference, where the MEAN, MAE, STD and RMS are calculated over a five-year period

Fig. 7 Statistical accuracy of the ZTD for VMF3-FC $5 \times 5°$ grid-wise products determined using the IGS-ZTD as a reference, where the MEAN, MAE, STD and RMS are calculated over a five-year period

compared for different sites in Figs. 5 and 6. Figure 5 clearly shows that the mean error of the ZTD products is also uniformly distributed globally. However, the deviation is relatively larger than that of the VMF3-FC site-wise approach, particularly in the Antarctic region.

A comparison of Figs. 5 and 6 clearly reveals that a considerably larger deviation for the ZTD in the Antarctic region than in other areas. This result suggests that tropospheric errors in the Antarctic are influenced primarily by the ZHD. This effect may be attributed to the polar vortex phenomenon unique to the Antarctic region. The polar vortex can cause considerable anomalies in the atmospheric pressure. Considering that the ZHD depends strongly on the atmospheric pressure, the pronounced deviation in the ZHD observed in this region likely reflects the impact of the polar vortex. As the latitude decreases, the accuracy of the VMF3-FC $1 \times 1°$ product decreases compared with the site-wise product.

Figures 7 and 8 show the statistical accuracy of the ZTD and ZWD for the VMF3-FC $5 \times 5°$ product. The larger grid size of the VMF3-FC $5 \times 5°$ product considerably reduces the accuracy of the calculated ZTD and ZWD. The atmospheric anomalies caused by the polar vortex in the Antarctic region have a pronounced impact on the ZHD. As a result, the error in the ZHD exceeds 5 cm at some IGS stations. The accuracy of both the VMF3-FC site-wise and grid-wise products clearly varies with the latitude.
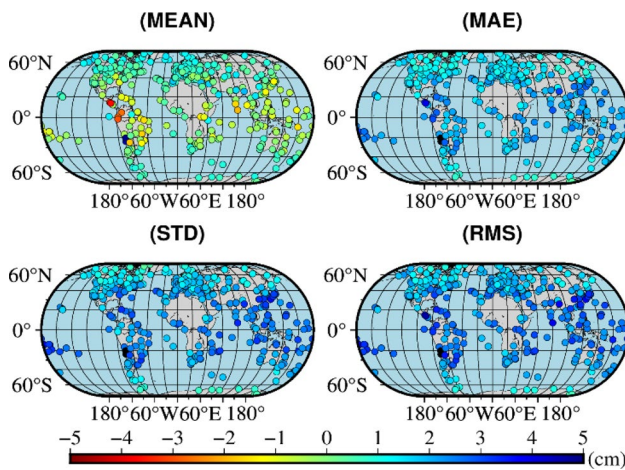
Fig. 8 Statistical accuracy for the ZWD for VMF3-FC 5×5° grid-wise product determined using the ZWD separated from IGS-ZTD as a reference, where the MEAN, MAE, STD and RMS are calculated over a five-year period

Table 2 shows the results of a statistical analysis of the errors of different products. The mean errors of the ZTD and ZWD for different products are within 0.4 cm. The accuracy of the site-wise product is considerably greater than that of the grid-wise product, with the 5×5° grid-wise product exhibiting the lowest accuracy. For both the site-wise and 1×1° grid-wise products, the average RMS is within 1.7 cm and the maximum RMS is only 3.86 cm. By contrast, the 5×5° grid-wise product has an average RMS exceeding 2.2 cm, with a maximum ZTD RMS of 5.71 cm and a maximum ZWD RMS of 7.07 cm.

Establishment of a prior variance model

It is critical to determine an appropriate a priori variance to optimize the VMF3-FC performance. Typically, the a priori variance for the forecast ZTD is set at an empirical value of 2~3 cm. However, an experimental analysis suggests that it may be insufficient to use this empirical value. To optimize the use of VMF3-FC products, it is essential to apply a variance suitable for the specific product. The strong correlation between the VMF3-FC errors and geographical location may make it unsuitable to apply a single global variance.

Therefore, the correlation between VMF3-FC errors and the geographic location should be analyzed to develop a more accurate a priori variance model. To analyze how the VMF3-FC varies with the geographical location, error sequences were plotted for the latitude, longitude, and height of IGS stations and fitted with different functions. Figures 9, 10 and 11 show the changes in the accuracies of the sequences of the VMF3-FC site-wise, grid-wise 1×1°, and 5×5° products with the geographical location.

Figure 9 clearly shows that the error for the VMF3-FC site-wise product is uniformly distributed between 0 and 3 cm for randomly distributed IGS stations. An analysis of the sequence on the basis of the latitudinal variation of the sites clearly shows that with increasing latitude, the RMS of the VMF3-FC site-wise product first increases and then decreases, reaching a maximum near the equator. By contrast, the RMS increases slightly with the longitude, where the magnitude of the overall increase is considerably smaller than the change in the RMS with the latitude. Figure 9 shows that the accuracy of the VMF3-FC site-wise products increases with the station height. This improvement may be attributed to the tropospheric influence being confined to heights of approximately 50 km. The air becomes
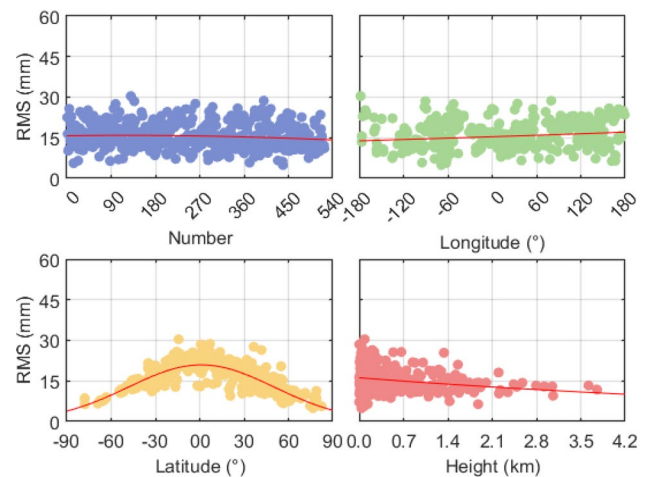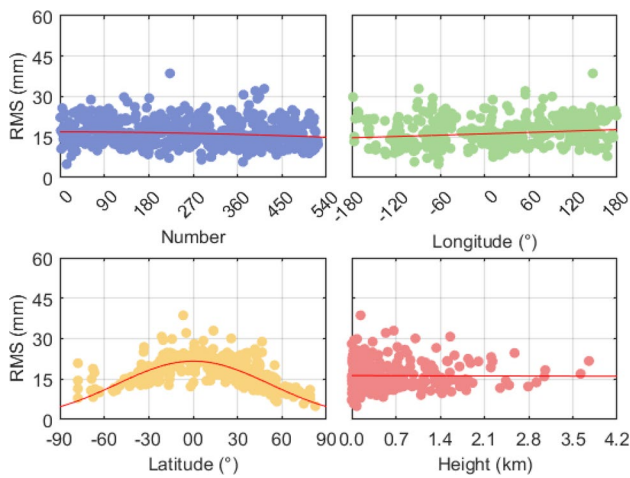

Fig. 9 VMF3-FC site-wise ZTD RMS distributions of IGS stations over a period of 5 years. The four subplots show the error sequence for the station randomness, latitudinal variation, longitudinal variation, and height variation

Table 2 Statistical accuracy of the VMF3-FC site-wise, grid-wise 1×1° and 5×5° products determined using global IGS stations as the statistical sites for a duration of 5 years (units: cm)

Type	MEAN	MAE	STD	RMS	Max-RMS	Min-RMS
Site-ZTD	0.05	1.17	1.49	1.55	3.04	0.49
Site-ZWD	0.32	1.25	1.48	1.63	3.07	0.53
Grid1-ZTD	0.01	1.25	1.54	1.63	3.86	0.50
Grid1-ZWD	0.38	1.31	1.51	1.68	3.78	0.53
Grid5-ZTD	-0.12	1.72	2.07	2.23	5.71	0.22
Grid5-ZWD	0.35	1.73	2.04	2.24	7.07	0.53

Fig. 10 Five-year ZTD RMS distributions of the VMF3-FC grid-wise $1 \times 1°$ product at IGS stations are shown in the four subplots for the error sequence for the station randomness, latitudinal variation, longitudinal variation, and height variation
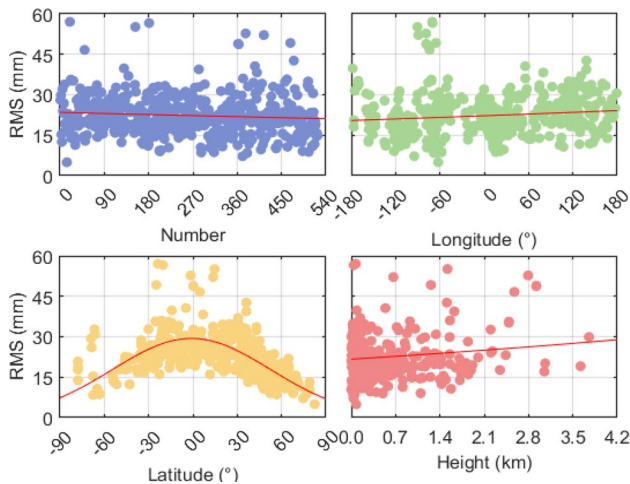
Fig. 11 VMF3-FC grid-wise $5 \times 5°$ ZTD RMS distributions of IGS stations worldwide over the past 5 years. The four subplots show the random distribution of stations, as well as error sequence maps of latitudinal, longitudinal, and height changes

progressively thinner with increasing height, reducing tropospheric errors.

Figures 10 and 11 show the distribution characteristics of the ZTD accuracy for the grid-wise $1 \times 1°$ and $5 \times 5°$ products with respect to the geographical location. The grid-wise product, in particular the $5 \times 5°$ product, has a lower accuracy than the VMF3-FC site-wise product. However, the grid-wise product exhibits the same error variation pattern with the longitude and latitude as the site-wise product.

The subgraph of the RMS variation with the latitude clearly shows that, compared with the results for the site-wise product, the grid-wise distribution gradually becomes

more divergent as the grid size increases, especially between $-70°$ and $-90°$. This increased divergence is probably caused by anomalous atmospheric pressure conditions in the Antarctic region. As the grid size increases, the ZTD accuracy gradually trends downward in the height. This trend may be attributed to the use of grid points for the tropospheric interpolation of IGS stations. If there is a large variation in terrain heights across the area, height-related errors may be introduced despite the use of a model for height correction during the interpolation process, which may slightly reduce the VMF3-FC accuracy (Lei et al. 2024).

The results presented above clearly show that the longitude and height have a relatively minor effect on the accuracy of VMF-FC3, which can be dominated by the effects attributed to the latitude. On the basis of these findings, a tropospheric prior variance model considering the latitude was established. An extensive experimental analysis showed that the Gaussian function best fit the trend of the error sequence. Therefore, we used the Gaussian function to construct a reasonable prior variance model that is dependent on the latitude of the observation station, as given in (13):

$$ZTD_e = a \bullet \exp\left(-((B - b)/c)^2\right) \tag{13}$$

where a, b, and c are coefficients to be fitted; B is the station latitude, in degrees; and ZTD_e is the fitted residual for the measuring station, in centimeters. Table 3 shows the calculated optimal fitting coefficients and the corresponding residuals.

Table 3 shows that the fitting residual tends to increase with the grid spacing. The VMF3-FC site-wise is only 0.27 cm, whereas the $1 \times 1°$ and $5 \times 5°$ grid angles are 0.32–0.58 cm, respectively. The fit is mainly influenced by the error distribution, where the narrower the error distribution is, the better the fit is.

Positioning validation

To verify the accuracy of the latitude-based VMF3-FC priori variance model, 20 globally distributed stations were selected with uniform spatial coverage, as shown in Fig. 12, for PPP/PPP-IAR validation. In this experiment, IGS observational data from DOY 295 to 301 in 2024 were utilized

Table 3 Latitude-dependent VMF3-FC site-wise, grid-wise $1 \times 1°$ and $5 \times 5°$ product accuracies and Gaussian function fitting coefficients

| Coefficient	a	b	c	Residual (cm)
Site-wise	2.093	0.1042	6.988	0.2726
Grid-wise $1 \times 1°$	2.166	0.0184	7.299	0.3247
Grid-wise $5 \times 5°$	2.937	-0.0968	7.575	0.5757
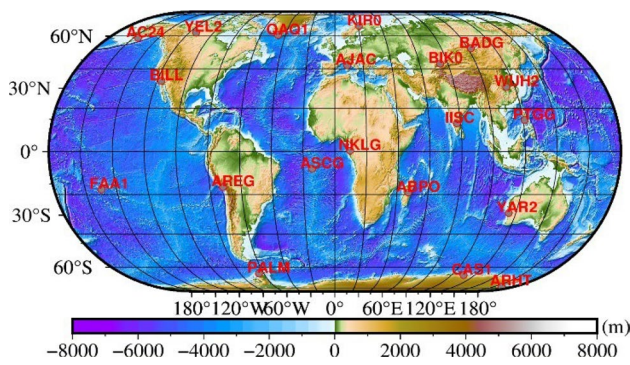
Fig. 12 Global distribution map of the positioning test stations

with a 30-s sampling interval and subjected to hourly PPP/PPP-IAR reconvergence process. The SINEX-derived IGS station coordinates served as reference coordinates.

During data processing, different resolution grid-wise (1 × 1° and 5 × 5°) products of VMF3-FC were used to calculate the ZTD at IGS stations, and tropospheric virtual observation equations were incorporated into the observation equations, as given by (10). To investigate the potential impact and optimization effects of different tropospheric a priori variance settings on positioning performance, four different strategies were evaluated for the ZTD-augmented PPP/PPP-IAR solutions: 1) no tropospheric constraint (none); 2) a latitudinal variation-based a prior variance constraint (fit); 3) the true a prior variance constraint derived from statistical data at the site (true); 4) an empirical a prior variance constraint. Specifically, for the 1° VMF3-FC products, an empirical a prior variance constraint of 2-cm was applied (var2), whereas for the 5° VMF3-FC products, a 3-cm a prior variance constraint was deemed necessary (var3), due to its relatively lower precision.

Firstly, the statistical results of PPP/PPP-IAR convergence time, as well as pre-convergence and post-convergence accuracy in the horizontal and vertical components, are summarized in Table 4. The table headings 'Vari', 'C-T', 'H-A', 'H-B', 'U-A', and 'U-B' denote variance, convergence time, and pre-convergence (A) and post-convergence (B) accuracy for horizontal (H) and vertical (U) components. The convergence criteria for horizontal and vertical positioning accuracy are set to be within 10 cm, with continuity over 20 epochs. The 90th percentile convergence series of ambiguity-float PPP solutions, augmented by VMF3-FC grid-wise (1 × 1° and 5 × 5°) ZTD, are shown in Figs. 13 and 14, respectively.
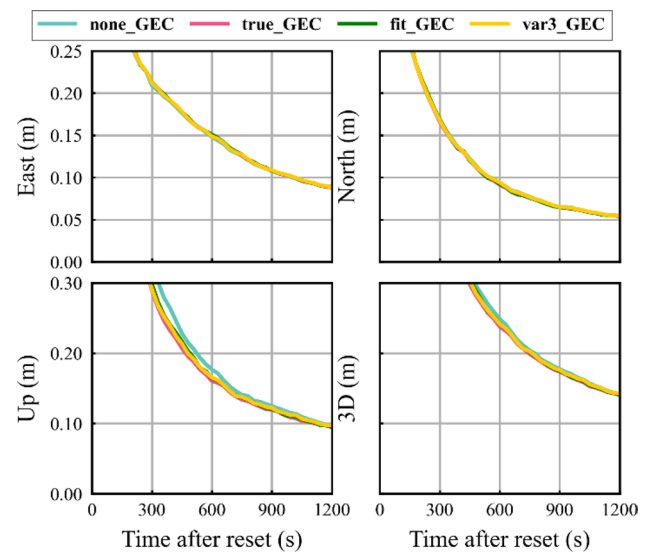
Fig. 13 Positioning errors (90th percentile) for ambiguity-float solutions obtained under 5 × 5° tropospheric constraints, including none, var3, fit, and true

Table 4 Statistical table of convergence time (s) and accuracy (cm) for positioning employing PPP for enhancing VMF3-FC products with different variances and resolutions

Mode	Vari	C-T(s)	H-A	H-B	U-A	U-B
PPP	none	809.224	16.039	4.166	17.953	3.703
	var2_1d	789.174	16.280	4.176	16.601	3.676
	fit_1d	788.437	16.246	4.156	16.806	3.658
	true_1d	788.201	16.239	4.161	16.804	3.671
	var3_5d	799.439	16.186	4.174	16.877	3.694
	fit_5d	797.658	16.140	4.160	17.060	3.683
	true_5d	792.145	16.230	4.170	16.924	3.684
	none	382.857	15.601	2.056	18.616	2.986
PPP-IAR	var2_1d	355.570	14.100	2.052	15.544	2.973
	fit_1d	348.813	14.164	2.051	15.402	2.970
	true_1d	346.394	14.200	2.052	15.425	2.970
	var3_5d	364.310	14.310	2.056	16.181	2.984
	fit_5d	356.362	14.313	2.053	16.007	2.980
	true_5d	353.914	14.258	2.053	15.903	2.973
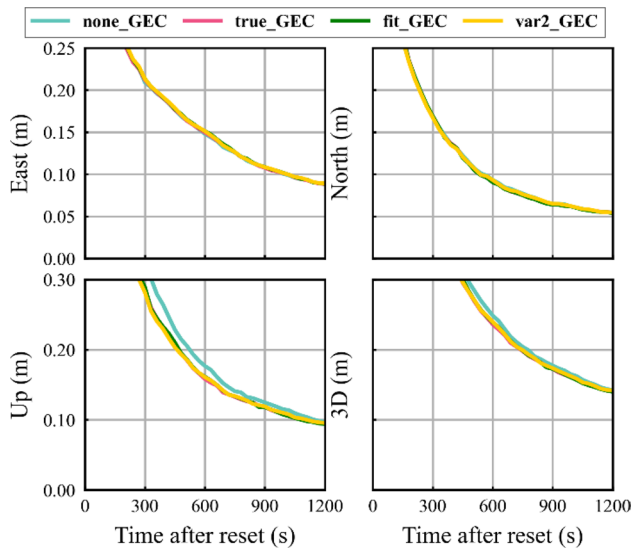
Fig. 14 positioning errors (90th percentile) for ambiguity-float solutions obtained under $1\times1°$ tropospheric products, including none, var2, fit, and true

The results show that implementing tropospheric constraints in PPP does not yield significant improvement for horizontal components. However, a notable enhancement is observed in the vertical component. Typically, the impact of ZTD corrections is noticeable primarily during the initial convergence phase, where these corrections mainly weaken the correlation with parameters in the vertical component. The $1\times1°$ VMF3-FC product demonstrates significantly better performance compared to the $5\times5°$ product, achieving

faster convergence due to its higher precision. However, different a priori variance models have minimal impact on performance. As shown in Table 4, the true variance and fitted variance provide only a slight improvement over the empirical variance, with an enhancement of less than 1%. This indicates that as long as variance values remain within a reasonable range, their influence on ambiguity-float PPP solutions is negligible.

Figures 15 and 16 further present convergence results for the PPP-IAR solution augmented by different tropospheric constraints, based on the application of VMF3-FC grid-wise $5\times5°$ and $1\times1°$ products. In contrast to the results presented in Figs. 13 and 14, the ZTD constraints begin to show positive effects on the horizontal components of the PPP-IAR solutions. This improvement is primarily due to the faster convergence rate of PPP-IAR and the effective decoupling of coordinates and ambiguity parameters, which makes the effect of the ZTD more pronounced during the early stages of convergence. However, once convergence is achieved, there seems to be minimal variation in the positioning results across different modes.

The comparison between Figs. 15 and 16 reveals that the higher accuracy of the $1\times1°$ product also lead to better convergence performance. Regardless of whether the $5\times5°$ or $1\times1°$ products are used, the empirical variance consistently provides the weakest constraint. In contrast, the 'true' and 'fit' methods yield nearly identical results, indicating that the variance derived from latitudinal fitting closely approximates the true variance obtained through statistical analysis.

In the PPP-IAR with tropospheric constraints, the tropospheric constraints can significantly impact ambiguity
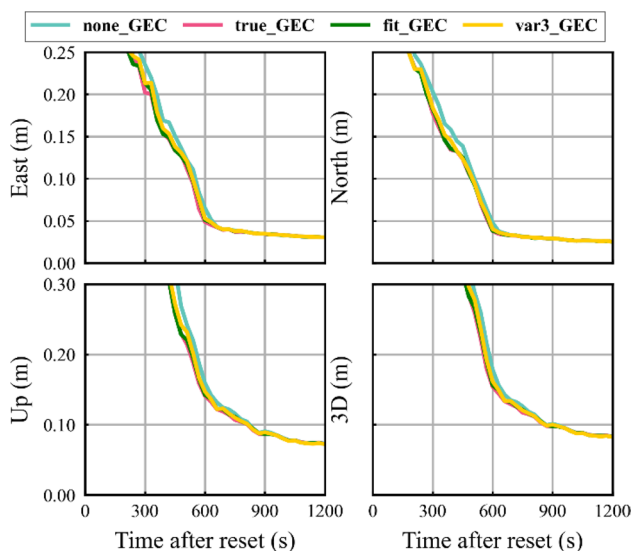
Fig. 15 Positioning errors (90th percentile) for ambiguity-fixed solutions obtained under $5\times5°$ tropospheric constraints, including none, var3, fit, and true
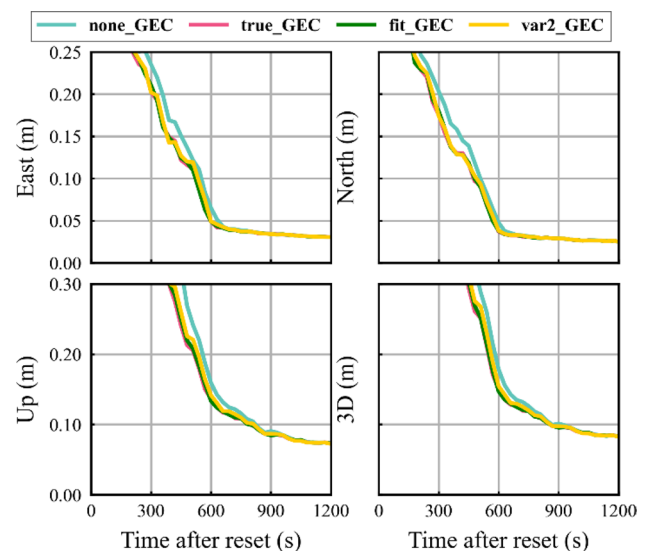
Fig. 16 Positioning errors (90th percentile) for ambiguity-fixed solutions obtained under $1\times1°$ tropospheric constraints, including none, var2, fit, and true

Table 5 Statistical analysis of PPP-IAR success fixed rate of ambiguity for VMF3-FC 1×1° grid-wise product constraints

	var2	fit	true
None	85.07%	85.07%	85.07%
ztd-augmented	86.41%	86.56%	86.56%
improvement percentage	1.34%	1.49%	1.49%

Table 6 Statistical analysis of PPP-IAR success fixed rate of ambiguity for VMF3-FC 5×5° grid-wise product constraints

	var3	fit	true
None	85.07%	85.07%	85.07%
ztd-augmented	86.08%	86.27%	86.32%
Improvement percentage	1.01%	1.20%	1.25%

resolution. Therefore, we have conducted a statistical analysis of the success fixed rate of ambiguity. The manuscript utilizes the cascading modified least-square ambiguity decorrelation adjustment (MLAMBDA) approach for ambiguity fixing, which involves sequential fixing of wide-lane and narrow-lane ambiguities. Given the absence of a direct criterion for the successful fixation of ambiguity, ambiguity resolution is considered successful when integer ambiguity is fixed and both horizontal and vertical positioning accuracies is within 10 cm.

It is worth noting that "Improvement" in Tables 5, 6 and 7 denotes an increase in the success rate for IAR, a reduction in convergence time, and an increase in positioning accuracy. Tables 5 and 6 provide the success fixed rate of ambiguity for PPP-IAR constrained by the 1×1° and 5×5° VMF3-FC grid-wise products, as well as the improvement percentage in success fixed rate compared to unconstrained PPP-IAR. It can be observed that the success fixed rate of ambiguity is above 85%, and the improvement in the success fixed rate for the 1×1° VMF3-FC product is higher than that for the 5×5° product. The improvement in the success fixed rate of ambiguity for the 1×1° VMF3-FC grid-wise product under the 'fit' and 'true' variance constraints is 1.49%, which is higher than the 1.34% improvement under the empirical

variance constraint. The improvements in the success fixed rate of ambiguity under the 'fit' and 'true' modes for the 5×5° product are 1.20% and 1.25%, respectively, which are slightly higher than the 1.01% improvement under the empirical variance constraint. Therefore, the success fixed rate of ambiguity also demonstrates that the precision of the 'fit' variance is markedly superior to that of the empirical variance and is close to the 'true' variance.

In addition to the success fixed rate of ambiguity, the final positioning accuracy was also statistically analyzed. The average of the last 30 epochs in each time period was taken as the final deviation. The results show that the final positioning accuracy is not affected by either the variance or the resolution of the VMF3-FC product. The precision of the final positioning results is consistent, with differences below the sub-millimeter level. The three-dimensional deviations in the East (E), North (N), and Up (U) directions are 1.21, 1.10, and 2.43 cm, respectively. This finding corroborates the conclusions drawn from Figs. 13, 14, 15 and 16, which indicate that the impact of tropospheric constraints is primarily evident during the initial phase of positioning. Once the positioning has converged, the influence of tropospheric constraints becomes negligible.

To comprehensively assess the enhancement of PPP-IAR positioning performance under varying variance configurations with tropospheric constraints, a statistical analysis was performed. This analysis specifically quantified the percentage improvements in positioning accuracy and convergence speed when tropospheric constraints were incorporated, as compared to scenarios where such constraints were absent. Table 7 shows the improvement in positioning accuracy under different tropospheric variances in the PPP-IAR mode. As can be seen from Table 7, both the convergence speed and positioning accuracy are notably improved in the PPP-IAR mode, consistent with the results shown in Figs. 15 and 16.

Specifically, PPP-IAR constrained by the 5×5° grid-wise product exhibited improved convergence over unconstrained PPP-IAR. Specifically, convergence enhancements of 4.8%, 6.9%, and 7.6% were achieved using the empirical, fitted, and true variance constraints, respectively. Using the empirical, fitted, and true variance constraints improved the pre-convergence accuracy in the horizontal component by

Table 7 Improvement percentage of convergence time and accuracy for positioning employing PPP for enhancingVMF3-FC products with different variances and resolutions

Mode	Vari	C-T(s)	H-A	H-B	U-A	U-B
PPP-IAR	var2_1d	7.13%	9.62%	0.19%	16.50%	0.44%
	fit_1d	8.89%	9.21%	0.24%	17.26%	0.54%
	true_1d	9.52%	8.98%	0.19%	17.14%	0.54%
	var3_5d	4.84%	8.28%	0.00%	13.08%	0.07%
	fit_5d	6.92%	8.26%	0.15%	14.01%	0.20%
	true_5d	7.56%	8.61%	0.15%	14.57%	0.44%
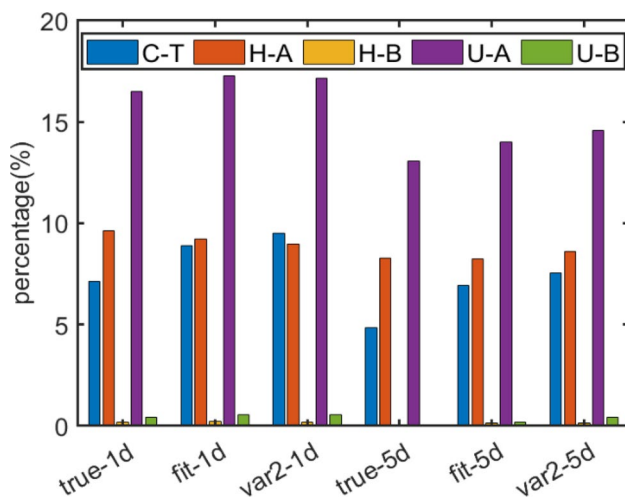
Fig. 17 Promote percentage of the convergence time and positioning accuracy of PPP-IAR, using unconstrained PPP-IAR as a reference

8.3, 8.3, and 8.6% and the pre-convergence accuracy in the vertical component by 13.1, 14.0, and 14.6%, respectively. Similarly, for PPP-IAR constrained with the $1 \times 1°$ grid-wise product, the convergence time was improved by using all variance models. Relative to the unconstrained condition, the improvement in the convergence time was 7.1% using the empirical variance, 8.9% using the fitted variance, and 9.5% using the true variance. Using the empirical, fitted, and true variance increased the pre-convergence accuracy by 9.6, 9.2, and 9.0 in the horizontal component, respectively, and by 16.5, 17.3, and 17.1%, respectively, in the vertical component. The influence of tropospheric constraints on the positioning results was minimal after convergence and could be neglected.

A comparison chart illustrating the improvement in positioning performance achieved through the application of VMF3-FC products with varying variances in the PPP-IAR mode is shown in Fig. 17. In this chart, the PPP-IAR results without ZTD constraints serve as the reference, with the promote percentages for other modes calculated relative to this baseline.

Conclusion

In this study, a five-year dataset spanning from 2019–2023 obtained using VMF3-FC and IGS-ZTD products was employed to assess the precision of various VMF3-FC products in estimating the ZTD and ZWD globally. The results showed that VMF3-FC site-wise products have substantially higher accuracy than grid-wise products do. The $1 \times 1°$ grid-wise product had considerably better precision than the $5 \times 5°$ grid-wise product did. The global average RMS values over five years for the three ZTD products were 1.53, 1.63,

and 2.23 cm. An analysis of the relationship between the RMS and station distribution revealed a strong correlation between the precision of the VMF3-FC product and the geographic station location. The latitude emerged as the most important factor affecting the accuracy. On the basis of these findings, a global prior variance model for VMF3-FC products was developed by fitting the RMS variations with the latitude. The global residuals for the variance models of the three products were 0.27, 0.32, and 0.57 cm, respectively.

To validate the prior variance model, 20 representative globally distributed stations were selected. The RMS ZTD for VMF3-FC at individual stations was used as the true variance and was compared with the fitted and empirical variances. This validate primarily investigates the performance of PPP-IAR positioning under different tropospheric prior variance constraints from three aspects: success fixed rate of ambiguity, convergence time, and positioning accuracy. Initially, a detailed analysis of the differences in ambiguity resolution success rate was conducted. The results indicate that, under conditions based on empirical variance, fitted variance, and true variance, the PPP-IAR scheme constrained by the $1 \times 1°$ grid product achieved respective improvements of 1.34, 1.49, and 1.49% in success fixed rate of ambiguity compared to the traditional method without tropospheric enhancement. These improvements are better than those obtained when constrained by the $5 \times 5°$ grid product, which only saw increases of 1.01, 1.20, and 1.25% under the same variance conditions. It can be seen that the PPP-IAR success fixed rate of ambiguity under the fitted variance constraint is comparable to that obtained using the true variance, whereas the empirical variance constraint enhanced PPP-IAR the least.

In terms of convergence speed and positioning accuracy. For PPP-IAR constrained with the $1 \times 1°$ grid-wise product, convergence times improved by 7.1, 8.9, and 9.5% under empirical variance, fitted variance, and true variance constraints, respectively, compared to the unconstrained condition. Pre-convergence horizontal accuracy improved by 9.6, 9.2, and 9.0%, respectively, and pre-convergence Up accuracy improved by 16.5, 17.3, and 17.1%, respectively. Similar conclusions can also be drawn from PPP-IAR constrained by $5 \times 5°$ grid-wise products. In addition to the above, the final positioning accuracy was also statistically analyzed. The results demonstrate that the impact of tropospheric constraints is primarily evident during the initial phase of convergence, with the influence on the final positioning results being at the sub-millimeter level.

In summary, the experimental results demonstrated that the variance derived from latitudinal fitting closely matched the true variance. Therefore, the variance model developed through latitudinal fitting is reliable at the global scale. This fitted variance can serve as the a priori variance for VMF3-FC products, effectively replacing empirical values

to exploit the potential of VMF3-FC more fully in real-time applications.

Declarations

Conflict of interest The authors declare that they have no known competing financial interests or personal relationships that could have appeared to influence the work reported in this paper.

References

Accadia C, Mariani S, Casaioli M, Lavagnini A, Speranza A (2003) Sensitivity of precipitation forecast skill scores to bilinear interpolation and a simple nearest-neighbor average method on high-resolution verification grids. Wea Forecasting 18(5):918–932. https://doi.org/10.1175/1520-0434(2003)018%3c0918:SOPFSS%3e2.0.CO;2

Askne J, Nordius H (1987) Estimation of tropospheric delay for microwaves from surface weather data. Radio Sci 22(3):379–386. https://doi.org/10.1029/RS022i003p00379

Berrada Baby H, Golé P, Lavergnat J (1988) A model for the tropospheric excess path length of radio waves from surface meteorological measurements. Radio Sci 23(6):1023–1038. https://doi.org/10.1029/RS023i006p01023

Bevis M, Businger S, Herring TA, Rocken C, Anthes RA, Ware RH (1992) GPS meteorology: remote sensing of atmospheric water vapor using the global positioning system. J Geophys Res 97(D14):15787–15801. https://doi.org/10.1029/92JD01517

Black HD (1978) An easily implemented algorithm for the tropospheric range correction. J Geophys Res 83(B4):1825–1828. https://doi.org/10.1029/JB083iB04p01825

Blewitt G (1990) An automatic editing algorithm for GPS data. Geophys Res Lett 17(3):199–202. https://doi.org/10.1029/GL017i003p00199

Boehm J, Heinkelmann R, Schuh H (2007) Short Note: a global model of pressure and temperature for geodetic applications. J Geod 81(10):679–683. https://doi.org/10.1007/s00190-007-0135-3

Böhm J, Möller G, Schindelegger M, Pain G, Weber R (2015) Development of an improved empirical model for slant delays in the troposphere (GPT2w). GPS Solut 19(3):433–441. https://doi.org/10.1007/s10291-014-0403-7

Byun SH, Bar-Sever YE (2009) A new type of troposphere zenith path delay product of the international GNSS service. J Geod 83(3–4):1–7. https://doi.org/10.1007/s00190-008-0288-8

Cui B, Wang J, Li P, Ge M, Schuh H (2022) Modeling wide-area tropospheric delay corrections for fast PPP ambiguity resolution. GPS Solut 26:56. https://doi.org/10.1007/s10291-022-01243-1

Du Z, Zhao Q, Yao W et al (2020) Improved gpt2w (igpt2w) model for site specific zenith tropospheric delay estimation in china. J Atmos Solar Terr Phys 198:105202

Gao R, Ye F, Liu Y, Zha J, Odolinski R, Satirapod C, Zhang B (2024) Optimizing ZWD estimation strategies for enhanced PPP-RTK performance. GPS Solut 28(2):86. https://doi.org/10.1007/s10291-024-01629-3

Hadas T, Teferle FN, Kazmierski K, Hordyniec P, Bosy J (2017) Optimum stochastic modeling for GNSS tropospheric delay estimation in real-time. GPS Solut 21:1069–1081. https://doi.org/10.1007/s10291-016-0595-0

Hersbach H, Bell B, Berrisford P et al (2020) The ERA5 global reanalysis. Quart J R Meteoro Soc 146(730):1999–2049. https://doi.org/10.1002/qj.3803

Hopfield HS (1969) Two-quartic tropospheric refractivity profile for correcting satellite data. J Geophys Res 74(18):4487–4499. https://doi.org/10.1029/JC074i018p04487

Huang L, Mo Z, Liu L, Zeng Z, Chen J, Xiong S et al (2021) Evaluation of hourly pwv products derived from era5 and merra-2 over the tibetan plateau using ground-based gnss observations by two enhanced models. Earth Sp Sci 8(5):e2020EA001516

Kouba J (2008) Implementation and testing of the gridded Vienna Mapping Function 1 (VMF1). J Geod 82(4–5):193–205. https://doi.org/10.1007/s00190-007-0170-0

Lagler K, Schindelegger M, Böhm J, Krásná H, Nilsson T (2013) GPT2: Empirical slant delay model for radio space geodetic techniques. Geophys Res Lett 40(6):1069–1073. https://doi.org/10.1002/grl.50288

Landskron D, Böhm J (2018) VMF3/GPT3: refined discrete and empirical troposphere mapping functions. J Geod 92(4):349–360. https://doi.org/10.1007/s00190-017-1066-2

Lei X, Xu X, Tao J, Yang T, Zhao Q, Guo J (2024) High-precision tropospheric correction method for NRTK regions with significant height differences. Meas Sci Technol 35(10):106315. https://doi.org/10.1088/1361-6501/ad6343

Li J, Yang F, Yuan D, Wang H, Song S, Tan J, Wen Z (2024) Unraveling the accuracy enigma: investigating ZTD data precision in TUW-VMF3 and GFZ-VMF3 products using a comprehensive global GPS dataset. IEEE Trans Geosci Remote Sens 62:1–10. https://doi.org/10.1109/TGRS.2024.3385228

Li XX, Wang B, Li X et al (2022) Principle and performance of multi-frequency and multi-GNSS PPP-RTK. Satell Navig 3:7. https://doi.org/10.1186/s43020-022-00068-0

Xiaoyang L (2020) Research on Key Parameters of Ground based GNSS Water Vapor Detection. China University of Mining and Technology, Jiangsu

Lu C, Zhang X, Zheng Y, Liu C, He B (2024) Real-time high-resolution tropospheric delay mapping based on GFS forecasts and GNSS. GPS Solut 28:175. https://doi.org/10.1007/s10291-024-01722-7

Lyu Z, Gao Y (2022) PPP-RTK with augmentation from a single reference station. J Geod 96:40. https://doi.org/10.1007/s00190-022-01627-8

Nafisi V, Urquhart L, Santos MC, Nievinski FG, Bohm J, Wijaya DD, Schuh H, Ardalan AA, Hobiger T, Ichikawa R, Zus F, Wickert J, Gegout P (2012) Comparison of ray-tracing packages for troposphere delays. IEEE Trans Geosci Remote Sens 50(2):469–481. https://doi.org/10.1109/TGRS.2011.2160952

Niell AE (1996) Global mapping functions for the atmosphere delay at radio wavelengths. J Geophys Res 101(B2):3227–3246. https://doi.org/10.1029/95JB03048

Noll CE (2010) The crustal dynamics data information system: a resource to support scientific analysis using space geodesy. Adv Sp Res 45(12):1421–1440. https://doi.org/10.1016/j.asr.2010.01.018

Osah S, Acheampong AA, Fosu C, Dadzie I (2021) Evaluation of zenith tropospheric delay derived from ray-traced VMF3 product over the West African region using GNSS observations. Adv Meteorol 2021:1–14. https://doi.org/10.1155/2021/8836806

Psychas D, Khodabandeh A, Teunissen PJG (2022) Impact and mitigation of neglecting PPP-RTK correctional uncertainty. GPS Solut 26:33. https://doi.org/10.1007/s10291-021-01214-y

re3data.org: VMF Data Server; editing status 2020–12–14; re3data.org - Registry of Research Data Repositories. https://doi.org/10.17616/R3RD2H

Sun P, Zhang K, Wu S, Wan M, Lin Y (2021) Retrieving precipitable water vapor from real-time precise point positioning using VMF1/VMF3 forecasting products. Remote Sens 13(16):3245. https://doi.org/10.3390/rs13163245

Santerre R (1991) Impact of GPS satellite sky distribution. Manuscr Geod 16:28–53

Saastamoinen J (1972) Contributions to the theory of atmospheric refraction. Bull Géod 105:279–298. https://doi.org/10.1007/BF02521844

Tao J, Chen G, Guo J, Zhang Q, Liu S, Zhao Q (2022) Toward BDS/Galileo/GPS/QZSS triple-frequency PPP instantaneous integer ambiguity resolutions without atmosphere corrections. GPS Solut 26(4):127. https://doi.org/10.1007/s10291-022-01287-3

Tao J, Chen G, Zhang G, Jiang Y, Kan H, Zhao Q (2024) Real-time regional tropospheric wet delay modeling and augmentation performance for triple-frequency PPP/PPP-IAR during typhoon weather. GPS Solut 28(2):96. https://doi.org/10.1007/s10291-024-01641-7

Teunissen PJG, Khodabandeh A (2015) Review and principles of PPP-RTK methods. J Geod 89(3):217–240. https://doi.org/10.1007/s00190-014-0771-3

Wu Z, Lu C, Tan Y et al (2023) Real-time GNSS tropospheric delay estimation with a novel global random walk processing noise model (GRM). J Geod 97:112. https://doi.org/10.1007/s00190-023-01780-8

Xu S, Yang Q, Du X, Xu X, Zhao Q, Yang L, Qin Y, Guo J (2024) Multi-GNSS precise point positioning enhanced by the real navigation signals from CENTISPACETM LEO mission. Adv Sp Res 73(8):4175–4186. https://doi.org/10.1016/j.asr.2024.01.017

Yang F, Guo J, Li J, Zhang C, Chen M (2021a) Assessment of the troposphere products derived from VMF Data server with ERA5 and IGS data over China. Earth Sp Sci 8(8):e2021EA001815. https://doi.org/10.1029/2021EA001815

Yang F, Meng X, Guo J, Yuan D, Chen M (2021b) Development and evaluation of the refined zenith tropospheric delay (ZTD) models. Satell Navig 2(1):21. https://doi.org/10.1186/s43020-021-00052-0

Yang L, Fu Y, Zhu J et al (2023) Overbounding residual zenith tropospheric delays to enhance GNSS integrity monitoring. GPS Solut 27:76. https://doi.org/10.1007/s10291-023-01408-6

Yuan Y, Holden L, Kealy A, Choy S, Hordyniec P (2019) Assessment of forecast Vienna Mapping Function 1 for real-time tropospheric delay modeling in GNSS. J Geod 93(9):1501–1514. https://doi.org/10.1007/s00190-019-01263-9

Zhang H, Chen L, Yang F, Ma J, Zhang J, Sun W, Xu S (2024) Evaluation of the zenith tropospheric delay (ZTD) derived from VMF3_FC and VMF3_OP products based on the CMONOC data. Atmosphere 15(7):766. https://doi.org/10.3390/atmos15070766

Zhang Q, Zhao Q (2018) Global ionosphere mapping and differential code bias estimation during low and high solar activity periods with GIMAS software. Remote Sens 10(5):705. https://doi.org/10.3390/rs10050705

Zhu G, Huang L, Yang Y, Li J, Zhou L, Liu L (2022) Refining the ERA5-based global model for vertical adjustment of zenith tropospheric delay. Satell Navig 3(1):27. https://doi.org/10.1186/s43020-022-00088-w

Xiaoting Lei received the master degree at Liaoning Technical University in 2023. he currently is a Ph.D. candidateat of Wuhan University. His main research interest is GNSS positioning and tropospheric modeling .

Jun Tao received his PhD degree in 2023 from Wuhan University,where he is currently a postdoc-toral fellow of Wuhan University.His current research mainly focuses on GNSS real-time precise positioning, real-time preciseclock estimation and GNSS augmentation and fast positioning .

Tianyu Yang received the master degree at Liaoning Technical University in 2021, where she is currently a Ph.D. candidateat of Liaoning Technical University. She works on GNSS positioning and its application .
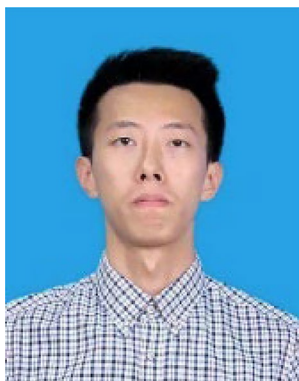
Gaojian Zhang is currently a Ph.D. candidate at GNSS Research Center, Wuhan University. He received his bachelor's degree and master's degree at Wuhan University in 2020, 2023. His current research interest is real-time high-precision positioning .

Jing Guo is a professor at the GNSS Research Center of Wuhan University. received the B.S. and Ph.D. degree in Geodesy and Surveying Engineering from Wuhan University, Wuhan, China, in 2009 and 2014, respectively. He works on GNSS data processing, particularly the precise orbit determination for LEO and GNSS satellites .

Qile Zhao is a professor at the GNSS Research Center of Wuhan University. He received his Ph.D. degree at Wuhan University in 2004. His current research interests are precise orbit determination of GNSS and low earth orbit satellites and high-precision positioning using GNSS .